Controlled Introduction of Diameter Modulations in Arrayed Magnetic Iron Oxide Nanotubes

Kristina Pitzschel,[†] Josep M. Montero Moreno,[†,‡] Juan Escrig,[§] Ole Albrecht,[†] Kornelius Nielsch,[†] and Julien Bachmann[†,*]

[†]Institute of Applied Physics, University of Hamburg, Hamburg, Germany, [‡]Electrodep, Departament de Química Física, Universitat de Barcelona, Barcelona, Spain, and [§]Departamento de Física, Universidad de Santiago de Chile, USACH, Chile

ABSTRACT To date, no large-scale preparative method for arrays of nanotube enables the experimentalist to arbitrarily define changes in the tubes' diameter along their length. To this goal, we start with anodic alumina substrates displaying controlled modulations in pore diameter obtained by alternating "mild" and "hard" electrochemical etching conditions. We then utilize atomic layer deposition (ALD) to coat the internal pore walls with conformal layers of an oxide. Ferromagnetic Fe_3O_4 tubes of 10 nm wall thickness and 10—30 μm in length are thus prepared, which replicate the modulated silhouette of the template. Their magnetic properties strongly depend on the presence of diameter modulations. Introducing one or several very short segments of large diameter (150 nm) into an otherwise thin tube (70 nm diameter) brings its initially large coercive field down to a value close to the case of a homogeneously thick tube. Theoretical modeling emphasizes the major influence of the magnetostatic interactions between neighboring tubes. They are enhanced locally at the sites of diameter modulations, which directly translates into a reduction in coercive field.

KEYWORDS: nanotubes · iron oxide · magnetism · diameter modulations · porous template

Considerable efforts have been invested in the past years into the development of methods for the preparation of pseudo-one-dimensional nano-objects with well-defined and homogeneous diameters.[1,2] Indeed, confinement effects (which by nature depend on geometry) are strongly affected by structural irregularities. Conversely, introducing changes in diameter in a controlled manner into nanowires or tubes should give rise to novel physical properties as well as novel possibilities to fine-tune them.[3,4] In the magnetism realm, diameter modulations should provide a handle over the motion of magnetic domain walls, a phenomenon proposed as a future data storage platform,[5] but the basic physics of which remain to be explored in detail. To date, no general method is available for the large-scale fabrication of such structures in ordered arrays.

To obtain wires or tubes with controlled diameter modulations, we propose to utilize as template the system reported recently in which porous alumina is obtained by combining "mild" and "hard" conditions of aluminum anodization.[6−8] In this letter, we demonstrate the possibility of exploiting this porous framework to create structures replicating the diameter modulations. Atomic layer deposition (ALD) is particularly suited to the conformal coating of the pore walls for the creation of tubes of oxidic materials,[9] given that it relies on a self-limiting chemical reaction at the surface. In fact, we contend that for the synthesis of inorganic nanotubes, ALD is superior to the other preparative approaches proposed to date (sol−gel coatings, direct coatings by surface chemistry in solution, epitaxial CVD coating of VLS wires, electrodeposition in pores, direct anodization of electropositive metals, and solvothermal crystallization of solids)[10−18] in terms of versatility and/or wall thickness control.

Thus, our preparation begins with an imprint which defines a perfectly ordered periodic structure on the aluminum surface. Subsequently, the aluminum is electrochemically oxidized under high voltage (70−100 V) to create the elongated pores. Key to the success of this step is the match between the periodicities of the imprint stamp, on the one hand, and of the self-ordering anodizations (hard and mild), on the other hand.[6,7] At last, homogeneous deposition of magnetic material into the pores is achieved by ALD. In this way, large arrays of parallel objects (10^8) are obtained with geometric parameters (length, width, and number of modulations) defined at the experimentalist's discretion.

EXPERIMENTAL RESULTS

Nanoimprinting of aluminum is the first step of our procedure (Scheme 1a).

*Address correspondence to julien.bachmann@physik.uni-hamburg.de.

Received for review August 1, 2009 and accepted September 24, 2009.

Published online October 5, 2009.
10.1021/nn900909q CCC: $40.75

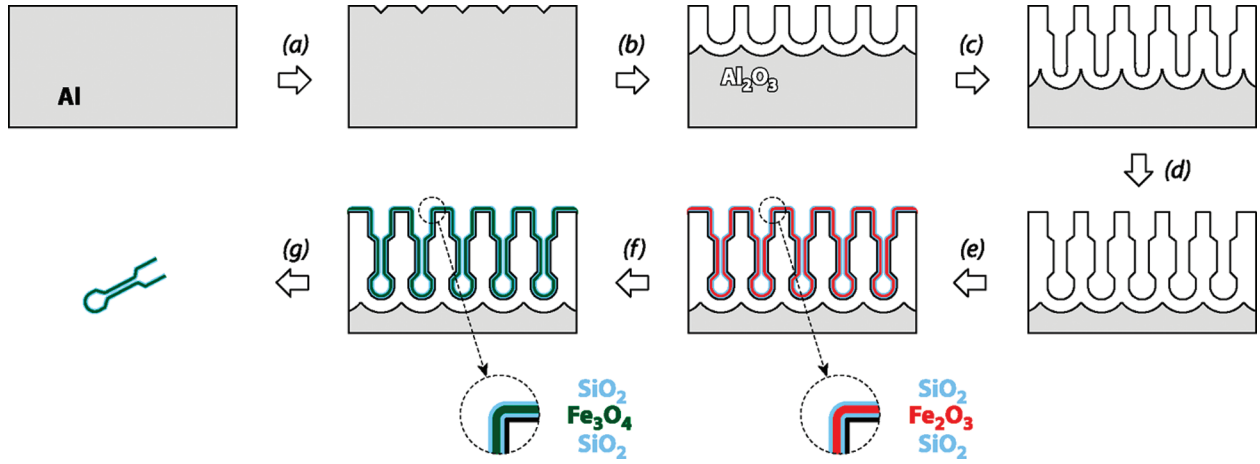

Scheme 1. Schematic presentation of the preparative steps for the creation of modulated magnetic nanotubes. (a) A polished Al chip is imprinted with a hexagonal pattern of 235 nm period; (b) mild anodization is performed under 72 V in phosphoric acid; (c) hard anodization follows under 93 V in oxalic acid; (d) mild and hard anodizations are repeated as needed to obtain the desired silhouette. (e) The pore walls are coated with successive layers of oxides by ALD: SiO_2, Fe_2O_3, and again SiO_2. (f) Reduction by H_2 at 400°C converts Fe_2O_3 to Fe_3O_4; (g) isolated tubes are optionally obtained for structural investigation by dissolution of the alumina matrix in chromic acid.

This pretexturing defines the subsequent nucleation of the pores during anodization. We used an imprint stamp consisting of hexagonally arranged SiN pyramids with a period of 235 nm. An electropolished aluminum chip was stamped with it under 9 tons mm^{-2}. For the subsequent anodizations (Scheme 1b−d), we adapted the applied voltages U to match the period $D_{int} = 235$ nm. The optimal voltages are $U_{mild} = 72$ V in phosphoric acid (0.40 M) and $U_{hard} = 93$ V in oxalic acid (0.15 M) for the mild and hard conditions, respectively. The former value deviates from the commonly accepted slope of the D_{int} *vs* U_{mild} curve (2.5 nm V^{-1}). We attribute this deviation to the comparatively very low voltage used here (72 V)—far from the self-ordered range of mild phosphoric acid anodization (160−196 V). Conversely, hard anodization is carried out at a drastically higher voltage (93 V) than usually done for the mild anodization in oxalic acid (40 V). In this case, stabilization of the unusually high electric field is achieved by combining two approaches: (1) formation of a thin oxide layer by a preliminary mild anodization, and (2) use of a water/ethanol mixture for hard anodization at −5 °C. This allows for the lithographically defined 235-nm order to be maintained throughout the anodization. Figure S1 in the Supporting Information compares the top and bottom sides of a 20 μm thick porous alumina membrane prepared under those conditions: the pores of 70 nm diameter and aspect ratio 300 have retained their large-scale perfectly periodic arrangement. Mild and hard anodizations yield different porosities (approximately 20% and 6%, respectively). Accordingly, they deliver distinct values of the pore diameter, namely, 150 and 70 nm. Therefore, several switches between the mild and hard conditions over the course of the anodization result in as many diameter modulations of the pores, as evident in Figure 1. The length L of each segment is controlled by the integrated current density Q passed through the system, with growth rates of $L_{mild}/Q = 0.3$ μm/(C/cm^2) and $L_{hard}/Q = 0.6$ μm/(C/cm^2) (for $Q \leq 20$ C/cm^2).

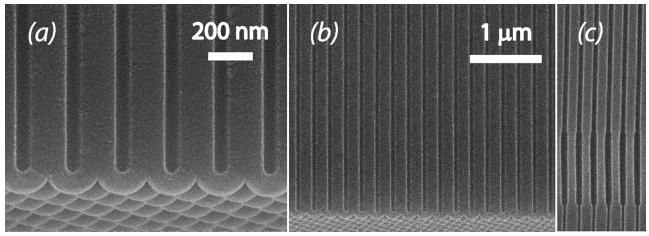

Figure 1. Scanning electron micrographs of a modulated porous anodic alumina template. The membrane is displayed in section; pores are broken in halves along their *z* axis: (a) end of the pores with hemispherical barrier layer; (b) the last 4 μm of a perfectly ordered "hard" segment; the pore diameter is absolutely constant and homogeneous; (c) a section of membrane displaying two changes in diameter, from "hard" anodization (narrow pores) to "mild" (thicker pores) and back to "hard"; the interfaces between the different segments are sharply defined. The scale bar is common for panels b and c.

The preparation of tubes of high aspect ratio (>1000) from this template implies coating the pores with a homogeneous thickness of the desired material without clogging their entrance. ALD (atomic layer deposition) is ideally suited to that purpose since it relies on a self-limited surface reaction between reactants provided in large excess from the gas phase. Indeed, applying our standard ALD reactions for Fe_2O_3 (from ferrocene and ozone)[19] and for SiO_2 (from 3-aminopropyltriethoxysilane, water, and ozone)[20] to the structured template yields multilayered $SiO_2/Fe_2O_3/SiO_2$ nanotubes embedded in the alumina membrane (Scheme 1e). Annealing the sample under Ar/H_2 at 400 °C converts Fe_2O_3 to the ferrimagnetic Fe_3O_4 (Scheme 1f). The silica layers enclosing the magnetic material in the resulting concentric $SiO_2/Fe_2O_3/SiO_2$ nanotubes (Figure 2b) serve

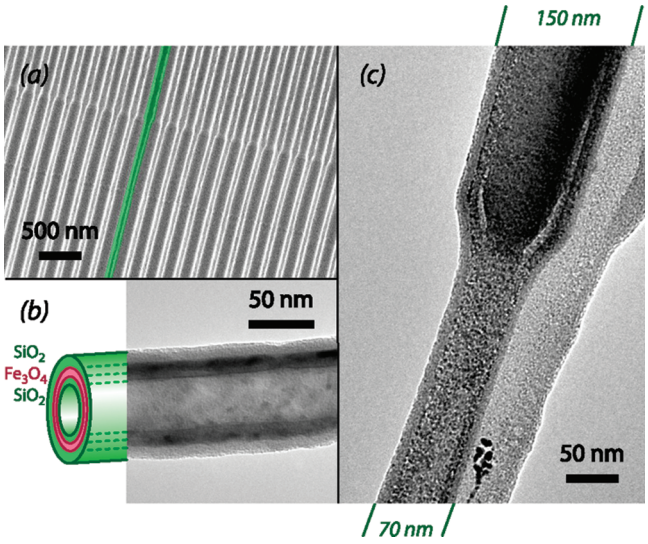

Figure 2. Structures of the modulated iron oxide nanotubes. (a) Scanning electron micrograph of a tube array imbedded in the alumina matrix, displayed in section; the tubes' walls appear white on the darker Al_2O_3 background, one tube was colored green for clarity. (b) Transmission electron micrograph of a Fe_3O_4 tube (after hydrogen reduction) protected by two thin silica layers. (c) TEM view of an isolated $SiO_2/Fe_2O_3/SiO_2$ tube (layer thicknesses: 6 nm/10 nm/6 nm) near a transition between a narrow segment and a wide one. Its silhouette reflects that of the arrayed objects from panel a.

two purposes. First, they act as chemically inert sheaths allowing for the dissolution of the alumina matrix (Scheme 1g) without damaging the magnetic objects. Second, they protect Fe_3O_4 from aerobic reoxidation. Modulated Fe_3O_4 tubes are displayed in Figure 2a,c. Electron microscopic investigation of the arrays shows the conformality of the deposition and the exact parallelism between the geometries of neighboring tubes. In transmission, isolated tubes display their multilayered structure, as well as clear transitions between the 70-nm wide "hard" segments and their 150-nm wide "mild" counterparts.

The nanotubes fabricated by this method behave ferromagnetically. As ensembles, they can be characterized in various orientations with respect to the applied field, as exemplified by the hysteresis loops of Figure 3a. When the sample is magnetized to saturation in a magnetic field H = 6 kOe applied along the long axis (z axis) of the tubes, $\vec{H}\|\vec{z}$, and the field is then turned off, 90% of the saturated magnetization is retained (remanence $\mu_{rem}^{\|} = 0.9\ \mu_{sat}$). In a perpendicularly applied field, $\vec{H}\perp\vec{z}$, the same experiment yields a remanence $\mu_{rem}^{\perp} = 0.4\ \mu_{sat}$. The large difference between $\mu_{rem}^{\|}$ and $\mu_{rem}^{\perp}$ defines z as the "easy" axis of the sample, as expected from the strong shape anisotropy. Accordingly, the effects of the diameter modulations can clearly be observed by the same method. Figure 3b summarizes the results of SQUID magnetic hysteresis loops recorded on five samples of Fe_3O_4 nanotube arrays with different types of diameter modulations (as shown in Figure 3c). The coercive field is only marginally affected by the geometry of the tubes when the field is applied $\vec{H}\perp\vec{z}$. In the $\vec{H}\|\vec{z}$ orientation, however, a monotonic increase emerges when the coercive fields are considered as a function of the hard/mild ratio. Tubes with smaller diameter (Figure 3c-E) have much larger values of $H_c^{\|}$ than the wider ones (Figure 3c-A). This is due to the more pronounced geometric anisotropy, as well as alleviated dipolar interactions between neighboring tubes.[21] More interestingly, comparing the last two samples (D and E on the right of Figure 3) reveals that the introduction of a single short wide segment in the middle of a long narrow tube causes

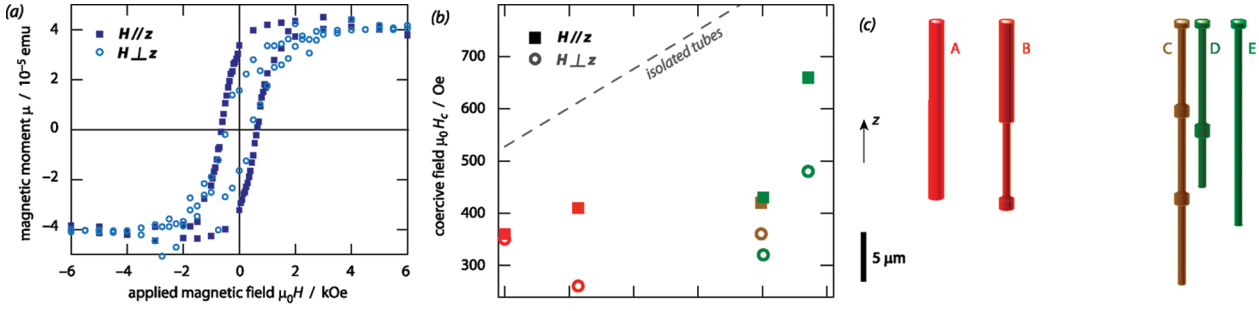

Figure 3. (a) Magnetic hysteresis loops of an array of Fe_3O_4 nanotubes (10 nm wall thickness) in a field applied parallel or perpendicular to the long axis (z axis) of the tubes at 300 K. Both the coercive field H_c (x intercept) and the remanence μ_{rem} (y intercept) are strongly affected by the orientation of the sample ($H_c^{\|}$ = 660 Oe; $H_c^{\perp}$ = 480 Oe; $\mu_{rem}^{\|} = 0.9\ \mu_{sat}$; $\mu_{rem}^{\perp} = 0.4\ \mu_{sat}$. Anodization conditions of the template: mild, 0.5 μm; hard, 20 μm. (b) Comparison of the coercive fields H_c of different types of modulated Fe_3O_4 tubes (as arrays). The uncertainty on H_c is evaluated as 50 Oe approximately. The experimental data points show a strong effect of geometry on H_c when the field is applied parallel to the long axis (full squares), in contrast to the case of H_c considered in the orthogonal orientation (empty circles). The gray line corresponds to coercive fields calculated for isolated objects as an interpolation between the values of thin and thick tubes. The x axis quantifies the volume fraction of magnetic material in the thin segment (from 0 to 1). Anodization parameters of the template: (A) mild, 15 μm; (B) mild, 10 μm −hard, 8 μm−mild, 1 μm; (C) mild, 0.5 μm−hard, 8 μm−mild, 1 μm−hard, 8 μm− mild, 1 μm−hard, 8 μm; (D) mild, 0.5 μm−hard, 10 μm−mild, 1 μm−hard, 5 μm; (E) mild, 0.5 μm−hard, 20 μm. (c) Schematic of the five geometries considered.

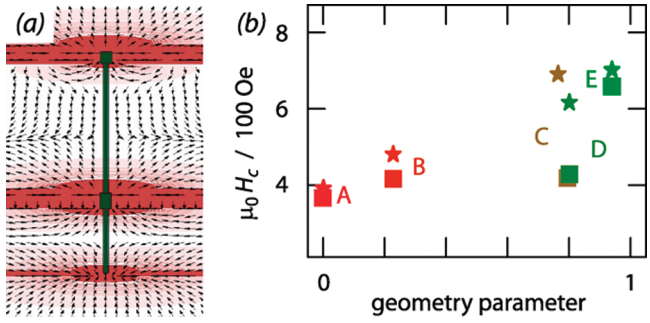

Figure 4. Theoretical modeling of the modulated magnetic tube arrays. (a) Stray field direction (arrows) and intensity (levels of red) generated by a modulated tube magnetized in the +z direction, as exemplified for structure D. (b) Coercive fields calculated for the different types of tubes, taking into account the strength of the dipolar interactions between neighboring tubes. The theoretical values (stars) are compared with the measured ones (squares). Labels A−E refer to the geometries described in Figure 3, and the geometry parameter equals the volume fraction of thin segments.

a drop in coercive field by more than 30%. This is a token that the diameter modulations influence the magnetic reversal phenomena beyond the linear regime.

THEORETICAL MODELING

This suspicion is corroborated by simple models of the magnetization reversal based on published methods. For isolated magnetic nanotubes, the magnetization reversal, that is, the change of the magnetization from one of its energy minima ($\vec{M} = M_0\hat{z}$) to the other ($\vec{M} = -M_0\hat{z}$), can occur by one of only three idealized mechanisms: a "coherent rotation" (**C**), defined by a simultaneous rotation of all spins (local magnetic moments), the "vortex mode" (**V**), whereby spins in rotation remain tangent to the tube wall, and the "transverse mode" (**T**), in which a net magnetization component in the (*x, y*) plane appears.[22] For any given geometry (diameter R and wall thickness d_w) of a long tube, coercive fields H_c can be calculated based on each mode from simple equations based on analytical models:[21] for **C**, the classical Stoner−Wohlfarth model,[23]

$$\frac{H_c^C}{M_0} = \frac{2(K(L) - K_a)}{\mu_0 {M_0}^2} \quad (1)$$

for **T**, an adapted version of it considering the width of the domain boundary w_T,[21]

$$\frac{H_c^T}{M_0} = \frac{2(K(w_T) - K_a)}{\mu_0 {M_0}^2} \quad (2)$$

and for **V**, the model proposed by Chang *et al.*,[24]

$$\frac{H_c^V}{M_0} = -\frac{2K_a}{\mu_0 {M_0}^2} + \alpha(\beta)\frac{{L_{ex}}^2}{R^2} \quad (3)$$

where K_a is the anisotropy constant, $K(l) = {}^1/_4\mu_0 {M_0}^2 (1 - 3N_z(l))$, $N_z(l)$ is the demagnetizing factor along z, $\beta = 1 - (d_w/R)$, and $L_{ex} = (2A/(\mu_0 {M_0}^2))^{1/2}$; the function $\alpha(\beta)$ is described in the reference. We use the material parameters $M_0 = 4.8 \times 10^5$ A m^{-3}, $A = 10^{-11}$ J m^{-1}, and $K_a = -11 \times 10^3$ J m^{-3}.[25] This analysis shows that of the three conceivable mechanisms for the magnetization reversal, **V** prevails (that is, yields the lowest values of H_c) for all geometries considered here (Figure S2). As expected, it also yields a larger H_c for the thinner ("hard") diameter than the thicker ("mild") one: $H_c = 530$ and 900 Oe for $R = 35$ and 75 nm, respectively, with $d_w = 10$ nm.

TABLE 1. Comparison of the Magnetostatic Interaction Energies E_{int} Calculated from eq 6 for Different Types of Nanotube Arrays[a]

tube type	$E^{ii}_{int}(d,0)$	normalized E_{int}
A	5.42×10^{-5}	(1)
B	1.20×10^{-4}	1.14
C	8.56×10^{-5}	1.34
D	1.80×10^{-4}	1.06
E	1.05×10^{-4}	0.63

[a]The values are then normalized to the amount of magnetic material and reported with respect to case A. Thin tubes (E) interact with their neighbors less strongly than thicker ones (A); additionally, the presence of short thick segments (C, D) introduces major increases in the interaction due to the nonvertical surfaces at the diameter modulations. The geometries A−E are as defined in Figure 3.

Considering a purely additive behavior of our samples combining mild and hard segments of tubes, one would expect a linear relationship between H_c and the relative amounts of thick and thin segments: it is the gray line of Figure 3b. Although the positive trend obtained in this way corresponds to the observations for samples A, B, and E, the calculated values are significantly higher than experimental ones. We ascribe these effects to the interaction of each tube with the stray field produced by its neighbors, which reduces the coercive field. Indeed, the stray field of a simple tube is most intense at its extremities, therefore in a modulated tube, the presence of additional nonvertical surfaces strongly reinforces the stray field at the modulations. This is shown in Figure 4a for the example of geometry D, and for all geometries in Figure S3. We can quantitatively compare the strength of the dipolar interaction between neighbors for various types of modulations by adding contributions for each pair of segments. The magnetostatic interaction of segment j with the stray field H_i generated by segment i in the neighboring tube of the tubes can be calculated from[26]

$$E_{int} = -\mu_0 \int \vec{M}_j(\vec{r}) \cdot \vec{H}_i(\vec{r})\, dv \quad (4)$$

Geometric considerations (presented in full detail in the Supporting Information) deliver the values of the interaction energy presented in Table 1 for the five types of tubes investigated experimentally, A−E. Even though thinner tubes intrinsically interact less strongly with one another than thicker ones do, this tendency can be overcome by the presence of diameter modulations: the nonvertical surfaces give rise to locally in-

tense stray fields and enhance the magnetostatic interaction between neighbors. The coercive field expected macroscopically for the ensemble is then reduced according to

$$H_c = H_c^V - H_{int} \quad (5)$$

where H_c^V denotes the intrinsic coercivity calculated for an isolated tube and H_{int} is the stray field within the array:[21]

$$H_{int} = \frac{2K(L)}{\mu_0 M_0}\left(\frac{\varepsilon|\tilde{E}_{int}^{ii}(d,0)|}{K(L)}\right)^{1/2} \quad (6)$$

Here, $\tilde{E}_{int}^{ii}(d,0) = E_{int}^{ii}(d,0)/(\mu_0 M_0^2 V)$ is the magnetostatic interaction between two identical nanotubes separated by an interaxis distance d.

Using eq 5 and eq 6 we can calculate the stray fields H_{int} and macroscopic coercive fields H_c for our array of nanotubes of geometries A−E. Because of the modulations, the stray field in the arrays may become significant (it increases from 140 Oe for A to 260 Oe for D). The final results are reported as stars in Figure 4b, along with the measured data points as squares. The agreement of the modeled values with the experiment is much improved as compared with the dashed gray line of Figure 3. Residual differences between calculated and measured values most likely originate from structural imperfections of the tubes prepared here, in particular the fact that the transition between thick and thin segments is not perfectly abrupt. Other factors not accounted for in our theoretical model include thermal effects, imperfect distribution of diameters, and the influence of finite lengths.

CONCLUSIONS

Our results demonstrate the validity of utilizing porous alumina as a template system for the creation of pseudo-one-dimensional nano-objects with the controlled introduction of changes in diameter. Such designed structural irregularities have consequences of prime importance on the magnetic characteristics of the tubes. Ensemble measurements combined with theoretical modeling enabled us to shed light onto the special properties of diameter changes with respect to the stray field of elongated magnetic nano-objects. In future studies, single-object measurements (magneto-optical Kerr effect, magnetic force microscopy) will be used to study the magnetic switching events in the individual segments, on the one hand, and in the absence of stray field, on the other hand. In this way, domain walls pinned at the structural irregularities could be observed.

But the preparative method delineated above is not limited to magnetic objects. Similar principles can be applied to the synthesis of modulated nanostructures with novel thermoelectric, electronic, or optical properties, as well. The ability to tune the modulations should enable one to highlight novel aspects of confinement in those areas of research.

METHODS

Preparation. Aluminum chips (99.999% from Goodfellow) are electropolished under +20 V in a 1−4 mixture of 60% $HClO_4$ and EtOH for 3 min. A stamp with hexagonally ordered SiN pyramids and a period of 235 nm is used to imprint the Al chips with a commercial hydraulic press under 9 tons mm^{-2}. The porous anodic alumina membrane is produced in several steps. The first anodization must be mild. Mild anodization is performed under 72 V in 0.4 M aqueous H_3PO_4 at 10 °C. The hard segments are anodized under 93 V in 0.15 M $H_2C_2O_4$ at −5 °C in a 4:1 water/ethanol mixture.[27] Atomic layer deposition of Fe_2O_3 and SiO_2 is performed in a Savannah 100 Reactor by Cambridge Nanotech according to the published procedures from ferrocene and ozone[19] and from 3-aminopropyltriethoxysilane, water, and ozone,[20] respectively.

Instrumental Methods. Scanning electron micrographs are taken on a Supra 55 or an Evo 50 by Zeiss under an acceleration voltage of 10 kV. Transmission microscopy was performed on a Jeol JEM1010 operating at 100 kV. TEM samples are prepared by dissolving the alumina matrix in an acidic 0.18 M Cr(VI) solution for 40 h at 45 °C, diluting the resulting suspension, and letting a drop of it evaporate on a holey carbon/Cu grid. The magnetic measurements are recorded at 300 K using a SQUID (superconducting quantum interference device) magnetometer MPMS2 by Quantum Design reaching magnetic fields between +50 and −50 kOe.

Acknowledgment. We thank D. Görlitz for insightful discussions and R. Meissner for crucial technical assistance. This work was supported by the German Research Council (DFG) in the framework of the Sonderforschungsbereich SFB668 "Magnetismus vom Einzelatom zur Nanostruktur" and by the German Ministry of Education and Research (BMBF FKZ03X5519). J.M.M. acknowledges the Comissionat per a Universitats i Recerca from the Departament d'Innovació, Universitats i Empresa from Generalitat de Catalunya, and the Fons Social Europeu for financial support. J.E. acknowledges the "Millennium Science Nucleus Basic and Applied Magnetism" (project P06-022F) and *Fondecyt* (project 11070010).

Supporting Information Available: Additional figures as mentioned in the text; geometric considerations delivering the dipolar interactions between neighboring tubes. This material is available free of charge *via* the Internet at http://pubs.acs.org.

REFERENCES AND NOTES

1. Xia, Y.; Yang, P.; Sun, Y.; Wu, Y.; Mayers, B.; Gates, B.; Yin, Y.; Kim, F.; Yan, Y. One-Dimensional Nanostructures: Synthesis, Characterization, and Applications. *Adv. Mater.* **2003**, *15*, 353–389.
2. Law, M.; Goldberger, J.; Yang, P. Semiconductor Nanowires and Nanotubes. *Annu. Rev. Mater. Res.* **2004**, *34*, 83–122.
3. Yang, C.; Zhong, Z.; Lieber, C. M. Electronic Properties by Synthesis of Axial Modulation—Doped Silicon Nanowires. *Science* **2005**, *310*, 1304–1307.
4. Hochbaum, A. I.; Chen, R.; Delgado, R. D.; Liang, W.; Garnett, E. C.; Najarian, M.; Majumdar, A.; Yang, P. Enhanced Thermoelectric Performance of Rough Silicon Nanowires. *Nature* **2008**, *451*, 163–167.
5. Parkin, S. S. P.; Hayashi, M.; Thomas, L. Magnetic Domain-Wall Racetrack Memory. *Science* **2008**, *320*, 190–194.

6. Lee, W.; Schwirn, K.; Steinhart, M.; Pippel, E.; Scholz, R.; Gösele, U. Structural Engineering of Nanoporous Anodic Aluminium Oxide by Pulse Anodization of Aluminium. *Nat. Nanotechnol.* **2008**, *3*, 234–239.
7. Lee, W.; Ji, R.; Gösele, U.; Nielsch, K. Fast Fabrication of Long-Range Ordered Porous Alumina Membranes by Hard Anodization. *Nat. Mater.* **2006**, *5*, 741–747.
8. Lee, W.; Scholz, R.; Gösele, U. A Continuous Process for Structurally Well-Defined Al_2O_3 Nanotubes Based on Pulse Anodization of Aluminum. *Nano Lett.* **2008**, *8*, 2155–2160.
9. Bachmann, J.; Jing, J.; Knez, M.; Barth, S.; Shen, H.; Mathur, S.; Gösele, U.; Nielsch, K. Ordered Iron Oxide Nanotube Arrays of Controlled Geometry and Tunable Magnetism by Atomic Layer Deposition. *J. Am. Chem. Soc.* **2007**, *129*, 9554–9555.
10. Lakshmi, B. B.; Patrissi, C. J.; Martin, C. R. Sol−Gel Template Synthesis of Semiconductor Oxide Micro- and Nano-structures. *Chem. Mater.* **1997**, *9*, 2544–2550.
11. Shenton, W.; Douglas, T.; Young, M.; Stubbs, G.; Mann, S. Inorganic−Organic Nanotube Composites from Template Mineralization of Tobacco Mosaic Virus. *Adv. Mater.* **1999**, *11*, 253–256.
12. Gong, D.; Grimes, C. A.; Varghese, O. K.; Hu, W. C.; Singh, R. S.; Chen, Z.; Dickey, E. C. Titanium Oxide Nanotube Arrays Prepared by Anodic Oxidation. *J. Am. Chem. Soc.* **2001**, *16*, 3331–3334.
13. Davis, D. M.; Podlaha, E. J. CoNiCu and Cu Nanotube Electrodeposition. *Electrochem. Solid State Lett.* **2005**, *8*, D1–D4.
14. Macak, J. M.; Tsuchiya, H.; Schmuki, P. High-aspect-ratio TiO_2 Nanotubes by Anodization of Titanium. *Angew. Chem., Int. Ed.* **2005**, *44*, 2100–2102.
15. Yu, H. D.; Zhang, Z. P.; Han, M. Y.; Hao, X. T.; Zhu, F. R. A General Low-Temperature Route for Large-Scale Fabrication of Highly Oriented ZnO Nanorod/Nanotube Array. *J. Am. Chem. Soc.* **2005**, *127*, 2378–2379.
16. Rao, C. N. R.; Govindaraj, A.; Deepak, F. L.; Gunari, N A.; Nath, M. Surfactant-Assisted Synthesis of Semiconductor Nanotubes and Nanowires. *Appl. Phys. Lett.* **2001**, *78*, 1853–1855.
17. Nath, M.; Rao, C. N. R. New Metal Disulfide Nanotubes. *J. Am. Chem. Soc.* **2001**, *123*, 4841–4842.
18. Jia, C. J.; Sun, L. D.; Yan, Z. G.; You, L. P.; Luo, F.; Han, X. D.; Pang, Y. C.; Zhang, Z.; Yan, C. H. Iron Oxide Nano-tubes—Single-Crystalline Iron Oxide Nanotubes. *Angew. Chem., Int. Ed.* **2005**, *44*, 4328–4333.
19. Bachmann, J.; Escrig, J.; Pitzschel, K.; Montero Moreno, J. M.; Jing, J.; Görlitz, D.; Altbir, D.; Nielsch, K. Size Effects in Ordered Arrays of Magnetic Nanotubes: Pick Your Reversal Mode. *J. Appl. Phys.* **2009**, *105*, 07B521.
20. Bachmann, J.; Zierold, R.; Chong, Y. T.; Hauert, R.; Sturm, C.; Schmidt-Grund, R.; Rheinländer, B.; Grundmann, M.; Gösele, U.; Nielsch, K. A Practical, Self-Catalytic Atomic Layer Deposition of Silicon Dioxide. *Angew. Chem., Int. Ed.* **2008**, *47*, 6177–6179.
21. Escrig, J.; Bachmann, J.; Jing, J.; Daub, M.; Altbir, D.; Nielsch, K. Crossover between Two Different Magnetization Reversal Modes in Arrays of Iron Oxide Nanotubes. *Phys. Rev. B* **2008**, *77*, 214421.
22. Landeros, P.; Allende, S.; Escrig, J.; Salcedo, E.; Altbir, D.; Vogel, E. E. Reversal Modes in Magnetic Nanotubes. *Appl. Phys. Lett.* **2007**, *90*, 102501.
23. Stoner, E.; Wohlfarth, E. C. Mechanism of Magnetic Hysteresis in Heterogeneous Alloys. *Philos. Trans. R. Soc. London, A* **1948**, *240*, 599.
24. Chang, C.-R.; Lee, C. M.; Yang, J.-S. Atomic-Structure and Electronic-Structure of Amorphous Si from First-Principles Molecular-Dynamics Simulations. *Phys. Rev. B* **1994**, *50*, 6461.
25. O'Handley, R. C. *Modern Magnetic Materials: Principles and Applications;* Wiley: Weinheim, Germany, 2000.
26. Aharoni, A. *Introduction to the Theory of Ferromagnetism*; Clarendon: Oxford, U.K., 1996.
27. Li, Y.; Zheng, M.; Ma, L.; Shen, W. Fabrication of Highly Ordered Nanoporous Alumina Films by Stable High-Field Anodization. *Nanotechnology* **2006**, *17*, 5101–5105.